Energy & Environmental Science

PAPER

View Article Online
View Journal

Cite this: DOI: 10.1039/c5ee01147g

Superior thermoelectric performance in PbTe–PbS pseudo-binary: extremely low thermal conductivity and modulated carrier concentration†

Di Wu,‡[ab] Li-Dong Zhao,[cd] Xiao Tong,‡[a] Wei Li,[ab] Lijun Wu,[e] Qing Tan,[f] Yanling Pei,[c] Li Huang,[ab] Jing-Feng Li,[f] Yimei Zhu,[e] Mercouri G. Kanatzidis*[d] and Jiaqing He*[ab]

Received 13th April 2015,
Accepted 19th May 2015

DOI: 10.1039/c5ee01147g

www.rsc.org/ees

Lead chalcogenides are dominant thermoelectric materials in the medium-temperature range due to their highly favorable electronic band structures and low thermal conductivities. An important system is the PbTe–PbS pseudo-binary, and its low thermal conductivity originates largely from the coexistence of both alloying and nanostructuring through phase-separation. To better understand the competition between the alloying and phase separation and its pronounced effects on the thermoelectric performance in PbTe–PbS, we systematically studied, *via* transmission electron microscopy (TEM) observations and theoretical calculations, the samples of Spark Plasma Sintered (SPSed) 3 at% Na-doped $(PbTe)_{1-x}(PbS)_x$ with x = 10%, 15%, 20%, 25%, 30% and 35%. The highest figure of merit, *viz.*, ZT ~ 2.3 was obtained at 923 K, when the PbS phase-fraction, x, was 20%, which corresponds to the lowest lattice thermal conductivity of the series. The consistently lower lattice thermal conductivities in the SPSed samples as compared with the corresponding ingots originates from the mesostructured nature of the former, which contributes significantly to their superior ZT. We also studied the onset of carrier concentration modulation at ~600 K, which leads to the observed saturation of electrical transport properties due to the diffusion and re-dissolution of excessive Na into the PbTe–PbS matrix. This carrier concentration modulation is equally crucial to achieve very high power factors (up to 26.5 μW cm^{-1} K^{-2} at 623 K) and outstanding thermoelectric performances in SPSed PbTe–PbS binaries.

Broader context

The conflict between the growing demands of energy and exhausting non-renewable fossil fuel resources has drawn the world's concern over the last few decades. Thermoelectric materials are of great interest because they represent a technique, which can directly tap the vast reserves of currently under-used thermal energy, in an environmentally friendly manner, and thus are deemed promising in waste heat recovery and active cooling. At present, the bottleneck that restricts the application of thermoelectric materials and technology is their relatively low figure of merit, ZT. Only with an average ZT that exceeds ~3.0, could a practically usable energy transfer efficiency, *i.e.*, 50% of Carnot efficiency, be achieved. Herein, we report a broad plateau of high ZT in a 3 at% Na-doped $(PbTe)_{0.8}(PbS)_{0.2}$ SPSed sample, with a peak value of ~2.3 at 923 K, which is the highest ever reported in the lead chalcogenides; moreover, we exhibit that only a delicate balance between alloying and precipitate scattering can result in an optimal phonon scattering effect. In addition, we propose a solid explanation, *i.e.*, carrier concentration modulation due to Na diffusion and re-dissolution, to elucidate the "abnormal saturation" of electrical transport properties at ~600 K.

Introduction

Thermoelectric materials can directly create electrical power from heat and have thus drawn growing research interest for decades.[1] The performance of a specific thermoelectric material is evaluated by a dimensionless figure-of-merit, $ZT = S^2\sigma T/\kappa$, where S is the Seebeck coefficient, σ is electrical conductivity, T is the absolute temperature, and κ is thermal conductivity. To achieve

[a] Department of Physics, South University of Science and Technology of China, Shenzhen 518055, China. E-mail: he.jq@sustc.edu.cn
[b] Shenzhen Key Laboratory of Thermoelectric Materials, Shenzhen, 518055, China
[c] School of Materials Science and Engineering, Beihang University, Beijing 100191, China
[d] Department of Chemistry, Northwestern University, Evanston, Illinois 60208, USA. E-mail: m-kanatzidis@northwestern.edu
[e] Condensed Matter Physics and Materials Science Department, Brookhaven National Laboratory, Upton 11973, USA
[f] Key Laboratory of New Ceramics and Fine Processing, School of Materials Science and Engineering, Tsinghua University, Beijing, 100084, China
† Electronic supplementary information (ESI) available. See DOI: 10.1039/c5ee01147g
‡ These authors contributed equally to this work.

a satisfactory thermoelectric performance, a thermoelectric material should have proper electronic structure to assure a high power factor, PF = $S^2\sigma$, and simultaneously, a very low thermal conductivity, κ. The family of lead chalcogenides PbQ (Q = Te, Se or S) are such examples of paradigmatic thermoelectric materials. The high band degeneracies in these materials[2,3] favor high Seebeck coefficients, while their narrow band gaps[2,4] indicate that suitable electrical conductivities can be achieved *via* doping; moreover, the intrinsic lattice thermal conductivities of PbQ can be lowered to very low levels considering their simple crystal structures (space group $Fm\bar{3}m$) due to the high anharmonicity of their bonds and the recently identified soft phonon behaviors of their lattices.[5,6] The power factors of p-type lead chalcogenides can be enhanced further by valence band structure engineering *via* the introduction of resonant states, *i.e.*, Tl-doped PbTe,[7,8] or tuning the band's degeneracy through alloying, *i.e.*, PbSe alloyed PbTe,[9] MgTe alloyed PbTe,[10] PbSe–PbS alloys,[11] and MnTe alloyed PbTe.[12] The lattice thermal conductivity can be lowered by various nanostructuring approaches, *e.g.*, *in situ* nanophase precipitation[10,13–15] and *ex situ* powder processing[16–18] (nanoinclusion or grain refining). In addition, the pseudo-binary systems, PbTe–PbSe,[19,20] PbTe–PbS[21,22] and PbSe–PbS,[11,23] also exhibit remarkable thermoelectric performances. Both PbTe–PbSe and PbSe–PbS were believed to be complete solid solutions, the low thermal conductivities of which largely result from the alloy scattering due to Te/Se and Se/S point defects, although recent transmission electron microscopy studies disclosed that nano-scale precipitates do exist in PbSe–PbS alloys.[23] In contrast, the PbTe–PbS system has a verified immiscibility gap between the PbTe and PbS phases[24] and exhibits phase separation, either in the form of nucleation and grain-growth processes, spinodal decompositions,[25,26] or an intermediate case,[27] depending on the relative phase fraction. The competition between alloying ($PbTe_{1-x}S_x$) and phase separation extremely engenders the complex microstructures of the PbTe–PbS system that results in very low lattice thermal conductivities in this binary, compared with both pristine PbTe and PbS.

To investigate the nature and evolution of the microstructure at a deeper level with a broader range of PbS fractions than our previous studies, we systematically studied 3 at% Na-doped $(PbTe)_{1-x}(PbS)_x$ SPSed samples (x = 10%, 15%, 20%, 25%, 30%, and 35%). Previous work on a more limited set of compositions focused on cast ingots rather than SPSed materials. We find that the material's thermoelectric performance can be further optimized because we can consistently achieve the lower values of lattice thermal conductivity than those of the corresponding ingots,[21] yet with similar power factors. Since the powder processing and all-scale hierarchical structuring[13,28] procedures performed on these materials tend to introduce extra point defects, nanostructures and strong interfacial potential between mesoscaled grains, our results confirm that a much higher ZT can be obtained in all-scale hierarchical structured systems. In this study, we find that the lowest thermal conductivity occurs at the nominal PbS-phase fraction of 20%, and we attribute this to the least complete phase separation[27] and more effective nanoprecipitate scattering as discussed in our calculations in the frame of Callaway model. The phase separation between PbTe and PbS not only evolves according to their relative phase fractions, but also are largely affected by their previous heat treatment;[27,29] therefore, we strictly applied the same heat treatment procedures for all samples. Finally, we studied the diffusion and re-dissolution of excess Na in the PbTe–PbS matrix grains[14] at temperatures over ~600 K. This creates an increment in the hole concentration and could be responsible for the observed saturation of Seebeck coefficients and electrical conductivities above 600 K. This amounts to carrier concentration modulation with temperature and helps to maintain the excellent thermoelectric power factors at high temperatures in the Na-doped PbTe–PbS system. As a result of all-scale hierarchical structuring and carrier concentration modulation, we achieved a ZT peak value of ~2.3 at 923 K in the 3 at% Na-doped $(PbTe)_{0.8}(PbS)_{0.2}$ SPSed sample, which is the highest value ever reported in lead chalcogenides.

Results and discussion

Transport properties

In Fig. 1, we plot the thermoelectric properties for the SPSed samples of the 3 at% Na-doped $(PbTe)_{1-x}(PbS)_x$ series. The electrical conductivities, σ, of all the samples decrease as the temperature increases from 300 K to 600 K but once the temperature exceeds 600 K, a maximum in the Seebeck and saturation in the electrical conductivity become evident, as seen in Fig. 1(a). The Seebeck coefficients, S, in Fig. 1(b), increase almost linearly from ~60–65 μV K^{-1} at 300 K to ~260–280 μV K^{-1} at 600 K, after which the slope is interrupted and they decrease slowly. The qualitative shape of this saturation behavior is not reminiscent of a bipolar diffusion associated with thermally induced band gap excitations and the creation of conduction band electrons; it has a more profound reason as will be revealed later in this article. The trends in electrical conductivity and Seebeck coefficient above 600 K in these SPSed samples are dissimilar to those typically reported for Na-doped PbTe,[21,30] PbS,[31,32] PbTe–PbSe[20] or K-doped PbTe–PbS,[22] whose σ and S all show smooth, gradual variations with temperature.

As we have pointed out in previous reports,[21] the 3 mol% Na used to dope these materials is far more than what is necessary to obtain the carrier concentrations observed in the samples ($0.5–1.0 \times 10^{20}$ cm^{-3}). The excess Na is believed to reside in the intergrain space and on the surfaces of nanoprecipitates.[14,26] We regard the abrupt saturation to be the result of the diffusion and re-dissolution of Na, which is confined at grain/phase boundaries at low temperature, into the grain matrix at high temperatures, as we detail in a later section. The σ values of the $(PbTe)_{1-x}(PbS)_x$ SPSed samples drop systematically as the content of PbS x increases from 10% to 35%, while the corresponding S values change little. Except for the sample with x = 35%, all the $(PbTe)_{1-x}(PbS)_x$ samples exhibit very similar power factors (PF), especially at high temperatures, as seen in Fig. 1(c). The peak values of PFs occur at 623 K and vary

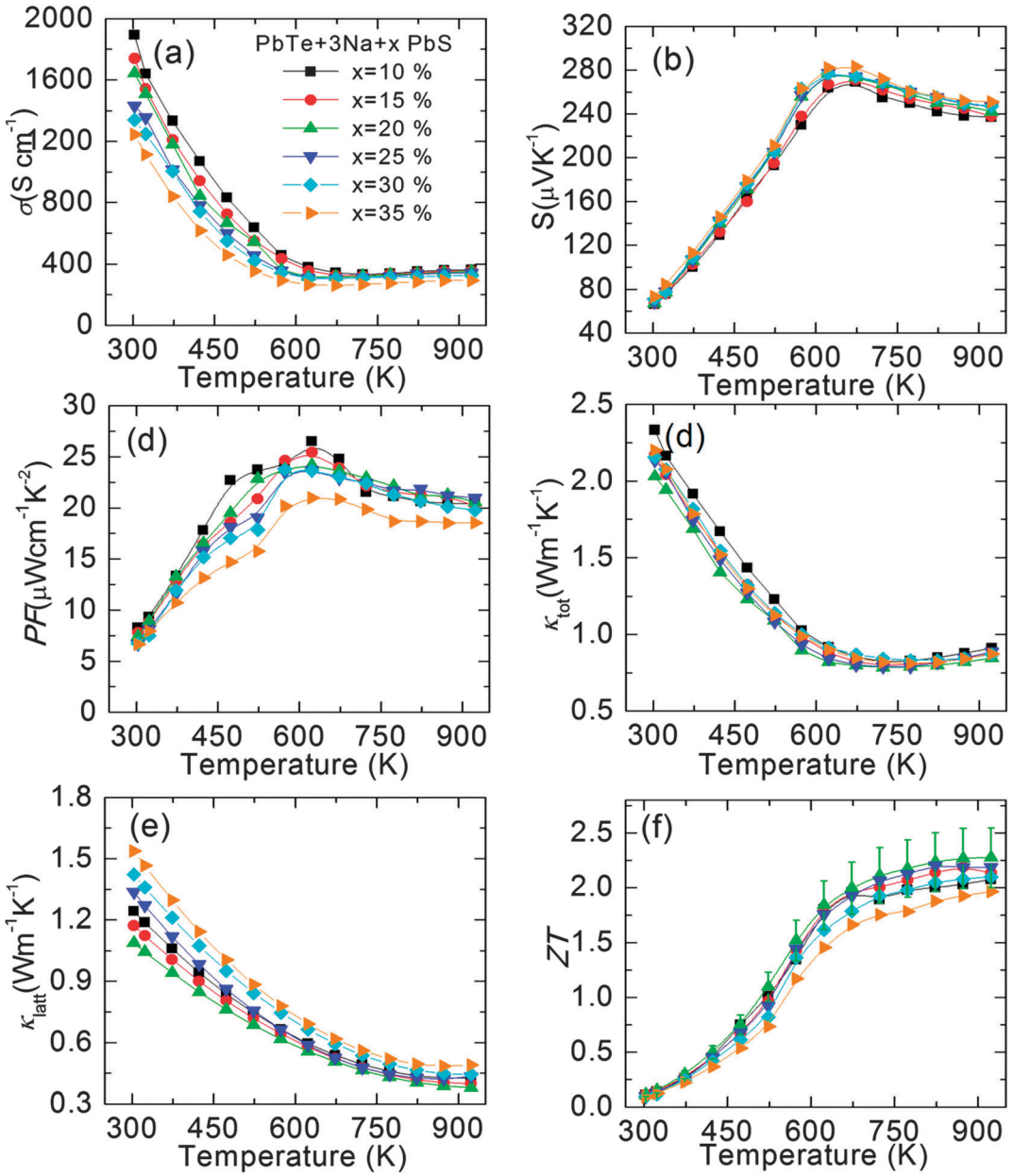

Fig. 1 (a) Electrical conductivities, (b) Seebeck coefficients, (c) power factors, (d) total thermal conductivities, (e) lattice thermal conductivities, and (f) figure of merit, ZT, of 3 at% Na-doped $PbTe_{1-x}S_x$ composites with x = 10%, 15%, 20%, 25%, 30% and 35%. For conciseness, we included the error bars of ZT for the x = 20% sample only.

from ~23.7 to 26.5 μW cm^{-1} K^{-2}, *viz.*, comparable to the highest reported values[9,14,21] in pristine PbTe systems.

The total thermal conductivities of different compositions are surprisingly close to each other, and all show a decreasing trend before 700 K where upturning starts, as seen in Fig. 1(d). Each lattice thermal conductivity is obtained by subtracting the electrical contribution from the total thermal conductivity, following the Wiedemann–Franz law as $\kappa_{latt} = \kappa_{tot} - \kappa_{ele}$, where $\kappa_{ele} = L\sigma T$ in which the Lorenz number, L, can be calculated from the reduced Fermi energy, ε_F, which is derived *via* the experimental Seebeck values as described elsewhere.[33,34] Fig. 1(e) shows that the lattice thermal conductivity is gradually suppressed with the increase of PbS content until x = 20%, thereafter it starts to increase. We show later that the lattice thermal conductivities observed for different PbS phase fractions, x, are closely related to their individual detailed microstructures. The values of lattice thermal conductivity range from 1.1 to 1.5 W m^{-1} K^{-1} at room temperature (303 K), and decrease to as low as ~0.38–0.45 W m^{-1} K^{-1} at 923 K. These high-temperature values of lattice thermal conductivity are so low that they even approach the "glass limit" of ~0.36 W m^{-1} K^{-1} for the bulk PbTe system as calculated by Cahill *et al.*[35] The high power factors over a broad temperature range (from 450 K to 923 K), together with the extremely low thermal conductivities,

result in a high ZT (>1.5) plateau in all samples from 600 K to 923 K (Fig. 1(f)), which indicate outstanding theoretical thermoelectric efficiencies[22] that are highly promising for commercial applications. Notably, a maximal ZT of ~2.3, which is one of the highest values[14,22,36,37] among thermoelectric bulk materials, was achieved in 3 at% Na-doped $(PbTe)_{1-x}(PbS)_x$ at 923 K for x = 20%.

Microstructure analysis

Powder X-ray diffraction patterns are presented in Fig. S2 (ESI†), which show that no extra phases other than PbTe and PbS were detected. It is obvious that the characteristic peak intensities of the PbS phase increase systematically as the nominal PbS content x changes from 10% to 35%; the fact that almost no PbS phases were found when the fraction of PbS is 10% implies an almost complete solid solution between PbTe and PbS. The characteristic peaks of the PbTe phase show no shift as x increases from 10% to 35%, which indicates a solution saturation of PbS in PbTe. The existence of a precipitated PbS secondary phase and the meso-scale homogeneity of our samples were validated *via* scanning electron microscopy, as shown in Fig. S3 (ESI†).

To explore the underlying physical mechanisms of the observed thermoelectric properties, we looked through the microstructural evolution of the 3 at% Na-doped $PbTe_{1-x}S_x$ (x = 10%, 20% and 30%) specimens with PbS fraction x. The 10% PbS sample exhibits the highest number density nanoscale precipitates with an average size of ~9 nm, Fig. 2(a). The inserted electron diffraction (ED) pattern, which covers a region with both precipitates and matrix, reveals an almost single set of reflections; this indicates endotaxy and small compositional and weak structural differences between the nanoscale precipitates and matrix. The statistical volume fraction of the precipitates (~23%) is much higher than the nominal PbS percentage of 10%, which implies that the precipitates are not a completely phase-separated PbS phase. Both lines of evidence suggest that the precipitated nanoparticles are somewhat richer in PbS than is the matrix; thus, the difference in mass density between the precipitates and the matrix is smaller than that between the pure PbS phase and the PbTe phase. Hence, phonon scattering from these precipitates appears to be weak (discussed in a later section) despite their high number density and small size. Cuboidal precipitates (118 nm, on average) were widely seen in the 20% PbS sample, which are shown in Fig. 2(b) and (c). The inserted ED pattern was obtained with an aperture that included the precipitate and the matrix. The two sets of split ED patterns were indexed separately as PbTe and PbS, which imply that the cuboidal precipitates are the completely phase-separated PbS. Moreover, the variance in composition between the precipitates and the matrix also was directly reflected by the Z-contrast difference in the STEM-HAADF (high-angle annular dark-field) image (Fig. 2(c)). Much larger precipitates, with an irregular round shape, (ranging from 200 to 800 nm, with an average of ~340 nm) were found in the 30% PbS sample, as seen in Fig. 2(d). This, along with the split ED patterns, provides strong evidence for the complete PbS phase separation from the PbTe–PbS solid solution.

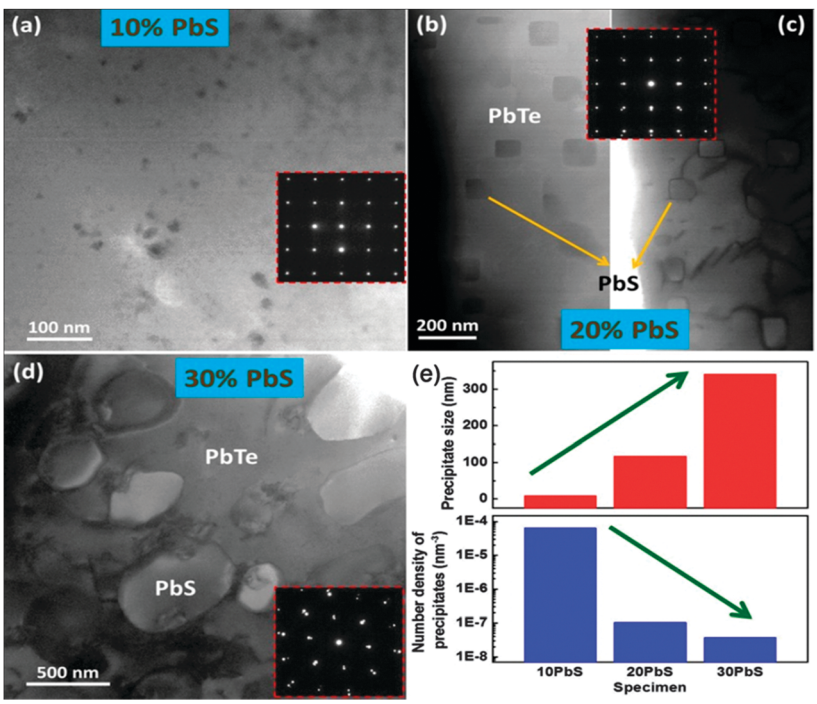

Fig. 2 (a) Low-magnification TEM image of the 10% PbS sample, which reveals nanoscale precipitates with inserted electron diffraction pattern along the [100] zone axis; (b) and (c) low-magnification TEM and STEM-HAADF images of the 20% PbS sample, which reveal cuboidal precipitates with inserted electron diffraction pattern along the [100] zone axis; (d) low-magnification TEM image of the 30% PbS sample shows large-scale precipitates with inserted electron diffraction pattern along the [110] zone axis; (e) the size and number density distribution histograms of precipitates for the 10%, 20%, and 30% PbS samples.

Considering the relatively large precipitates size compared to the typical wavelength of phonons (1–10 nm), which dominate thermal transport,[38] we do not expect an effective reduction of lattice thermal conductivity due to precipitate scattering. No obvious spinodal decomposition was observed in the 30% PbS sample, although this PbS phase fraction corresponds to the region of spinodal decomposition in the phase diagram.[24] This phenomenon could be explained by the significantly depressed coherent spinodal line as suggested by Doak *et al.*,[39] who originally included coherency strains in their density functional calculations and concluded that the depression in temperature of the spinodal line is so large that spinodal decomposition can only occur at very low temperatures, wherein it is probably kinetically unstable.

Statistical results, as shown in Fig. 2(e), reveal that the size of the precipitates increases as the number density decreases with the increase of the PbS fraction. Although the smallest size and highest number density of the precipitates were found in the 10% PbS sample, it was the 20% PbS sample that exhibits the lowest lattice thermal conductivity. The detailed relationship between microstructures and lattice thermal conductivities will be discussed later in our calculations. We note that these microstructural features of the SPS samples and their evolution with PbS content resemble what was reported in the corresponding ingots.[21,26]

We also employed the intermediate- and high-resolution STEM-HAADF and STEM-ABF (annular bright-field) techniques to study selected SPS samples (x = 10%, 20% and 30%). The interface between the S-rich precipitate (relatively darker in the HAADF imaging mode while brighter in the ABF imaging mode) and the PbTe matrix in the 10% PbS sample is indistinct, as shown in Fig. 3(a) and (b), which suggests a weak compositional gradient. Such a weak interface and composition contrast might be ineffective in scattering heat-carrying phonons. The cuboidal precipitates in the 20% PbS specimen exhibit regular Moiré fringes in thick areas, which are seen more clearly in the ABF image mode, as shown Fig. 3(c) and (d). It is well known that the Moiré pattern represents a type of diffraction contrast, due to the overlap between two sets of planes (*e.g.*, the PbS precipitate and the PbTe matrix from top to down) with nearly common periodicity and/or a small relative rotation angle. HAADF differs from the ABF imaging mode in STEM by its much smaller collection angles; thus, the HAADF imaging mode is more sensitive to compositional variations (so-called *Z*-contrast imaging), while the ABF mode exhibits high sensitivity to diffraction contrast. We observed clear interfacial contrast and misfit edge dislocations at the straight interfaces around the cuboidal precipitates, which are shown in Fig. 3(e) and (f). As the fraction of PbS further increases to 30%, much larger PbS particles then precipitate. It is apparent that the three samples show quite different microstructures, which could be derived from their disparate phase states in the PbTe–PbS binary phase diagram: the 10% PbS sample is located in the region of nucleation and growth, the 30% PbS sample lies in the region of spinodal decomposition, while the 20% PbS phase remains in between. The different microstructures are closely related to the charge and phonon transport properties, which are carefully treated in our calculations.

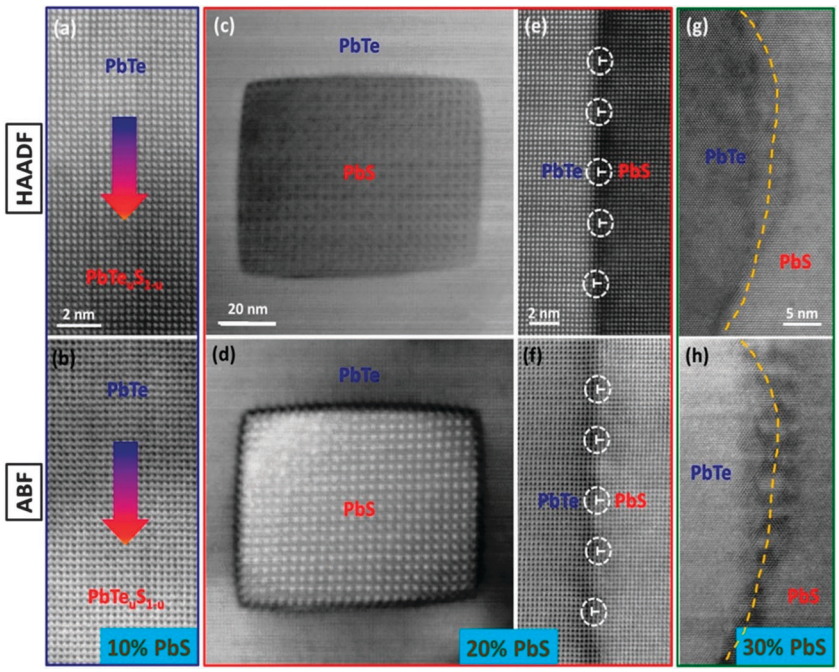

Fig. 3 Mediate- or high-resolution-STEM-HAADF (a, c, e, g) and STEM-ABF (b, d, f, h) images of the 10% (a, b), 20% (c–f), and 30% (g, h) PbS samples: (a) and (b) show the interface between the S-rich precipitate and the PbTe matrix, which lacks a clear interface; (c) and (d) shows regular Moiré fringes in a PbS cuboidal precipitate; (e) and (f) reflect the straight interface between the cuboidal PbS precipitate and the PbTe matrix with orderly arrayed dislocations; (g) and (h) reveal the round interface between a spherical PbS precipitate and the PbTe matrix.

Lowest lattice thermal conductivity in the x = 20% SPSed sample

It was seen earlier in Fig. 1(e) that the lattice thermal conductivity of 3 at% Na-doped $(PbTe)_{1-x}(PbS)_x$ decreases with x until it reaches 20%, and then increases again. To better illustrate this interesting behavior, we re-plotted the lattice thermal conductivity *versus* x (Fig. 4(a)) at 303 K, 623 K, and 923 K. The nominal composition of $(PbTe)_{0.8}(PbS)_{0.2}$ (x = 0.2) consistently exhibits the lowest lattice thermal conductivity at various temperatures, and the reason for this is not as trivial as it seems from the TEM observations. We ascribe the low lattice thermal conductivity of $(PbTe)_{0.8}(PbS)_{0.2}$ to the higher PbTe–PbS alloying ratio, as discussed by Girard *et al.*[21,27] together with effective phonon scattering by the nanoscale precipitates, and suggest that the incipient nano-precipitates (~10 nm) in $(PbTe)_{0.9}(PbS)_{0.1}$ (x = 10%) are relatively weak in scattering phonons, despite their small size.

To elucidate the relation of microstructure with lattice thermal conductivity in the 3 at% Na-doped $(PbTe)_{1-x}(PbS)_x$ SPSed samples, we now present thermal transport calculations based on the revised Callaway model, as described elsewhere.[29] As mentioned above, the grain sizes are mesoscale (>2 μm), and hence, the grain boundaries are fairly weak in scattering the short- and intermediate-wavelength phonons that dominate thermal transport. Moreover, although strains and dislocations might exist at phase/grain boundaries, they are not considered in our calculations since their number densities are low and difficult to be quantified precisely.[40] We include the contributions from the Umklapp scattering, the normal phonon–phonon scattering, and the point defects- and precipitates-scatterings in our calculations; detailed formulae and information are given in the ESI.†

In $(PbTe)_{0.9}(PbS)_{0.1}$, the matrix and the nanoprecipitates are believed to be sulfur-poor and sulfur-rich, respectively; however, as evidenced from the TEM observations mentioned above, the composition difference between them is small. This small composition contrast implies their inefficiency in phonon scattering despite the precipitates' small size and high number density, as suggested by eqn (S4) and (S5) (ESI†) and the literature.[40,41] In the spinodal decomposition region (x > 30%) of the PbTe–PbS phase diagram,[24] phase separation yields a PbTe-rich $PbTe_{0.93}S_{0.07}$ phase and a PbS-rich $PbS_{0.98}Te_{0.02}$ phase. In contrast, S alloying in PbTe can be as large as ~0.12 in the intermediate region (x − 16%) between nucleation-and-growth and spinodal decomposition in Na-doped PbTe–PbS composites, even after annealing, which indicates that this incompletely-phase-separated-state may be more thermodynamically preferred.[27,42] Our TEM statistics on the density and size of the precipitates confirm this argument and show that the volume fraction of PbS-rich precipitates in $(PbTe)_{0.8}(PbS)_{0.2}$ is only ~7% (in contrast to the nominal ~20% PbS fraction), which indicates a high alloying ratio of PbS as the result of incomplete phase separation. The reliability of our calculations is assessed by comparing the calculated results directly with experiments (Fig. 4(b)); note that the lattice thermal conductivities were calculated based on the volume fraction of the PbTe-rich and PbS-rich phases for both $(PbTe)_{0.8}(PbS)_{0.2}$ and $(PbTe)_{0.7}(PbS)_{0.3}$ with the phenomenological effective medium theory.[43,44] Within the margin of error, our calculated and experimental data reinforce the validity of our abovementioned argument that $(PbTe)_{0.8}(PbS)_{0.2}$ corresponds to an incomplete phase separation with large S alloying, and that the small nanoprecipitates widely found in $(PbTe)_{0.9}(PbS)_{0.1}$ show only small mass contrast from the matrix and cannot effectively scatter heat-carrying phonons.

Reduced thermal conductivity in the SPSed samples

Girard *et al.*[21] systematically studied the thermoelectric properties of Na-doped $(PbTe)_{1-x}(PbS)_x$ ingots, and reported very low

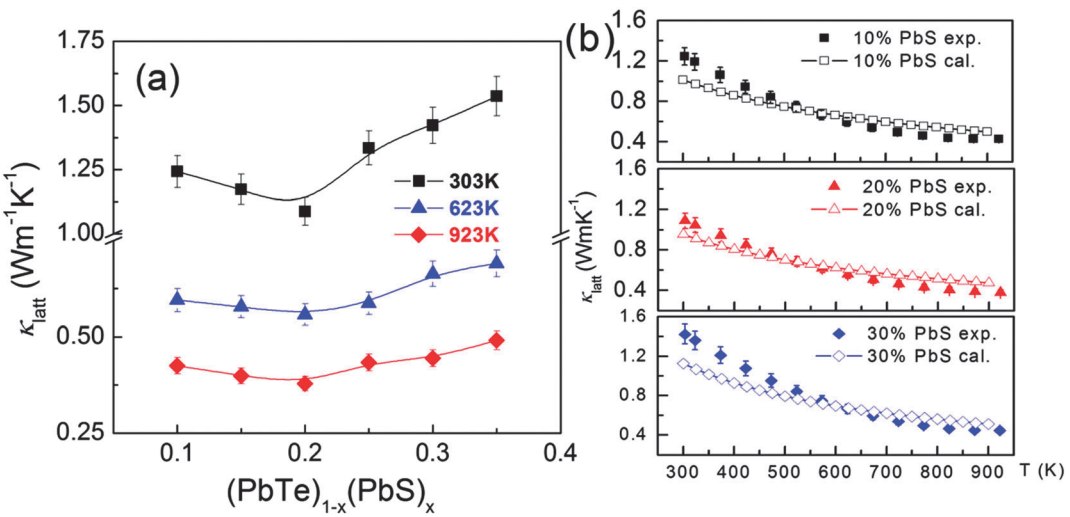

Fig. 4 (a) Lattice thermal conductivities (at 303 K, 623 K and 923 K) in $(PbTe)_{1-x}(PbS)_x$ samples decrease as x increases from 0.1 to 0.2, then increase with the elevating x value. (b) Calculated lattice thermal conductivities taking into account that the precipitates and alloying scattering (ESI†) match considerably with the experimental results. The data of x = 0.2 and 0.3 was calculated based on the volume fraction of the PbTe- and PbS-rich phases, with the phenomenological effective medium theory (EMT), which is described elsewhere.[43,44]

thermal conductivity after PbS alloying and Na-doping. Compared with the ingots (2 at% Na-doped $(PbTe)_{0.88}(PbS)_{0.12}$ was chosen due to its superior thermoelectric performance), the SPSed samples in our study exhibited very similar electrical conductivities and Seebeck coefficients, as depicted in Fig. 5(a) and (b). Moreover, the trends of the temperature dependent Hall carrier concentration, p, and mobility, μ, also are consistent with those of the ingots[21] (z at% Na-doped $(PbTe)_{0.88}(PbS)_{0.12}$ with z = 1.0, 1.5 and 2.0), as shown in Fig. 5(c), (d) and Table 1. As we know, the abrupt rise of hole concentration, p, that is derived

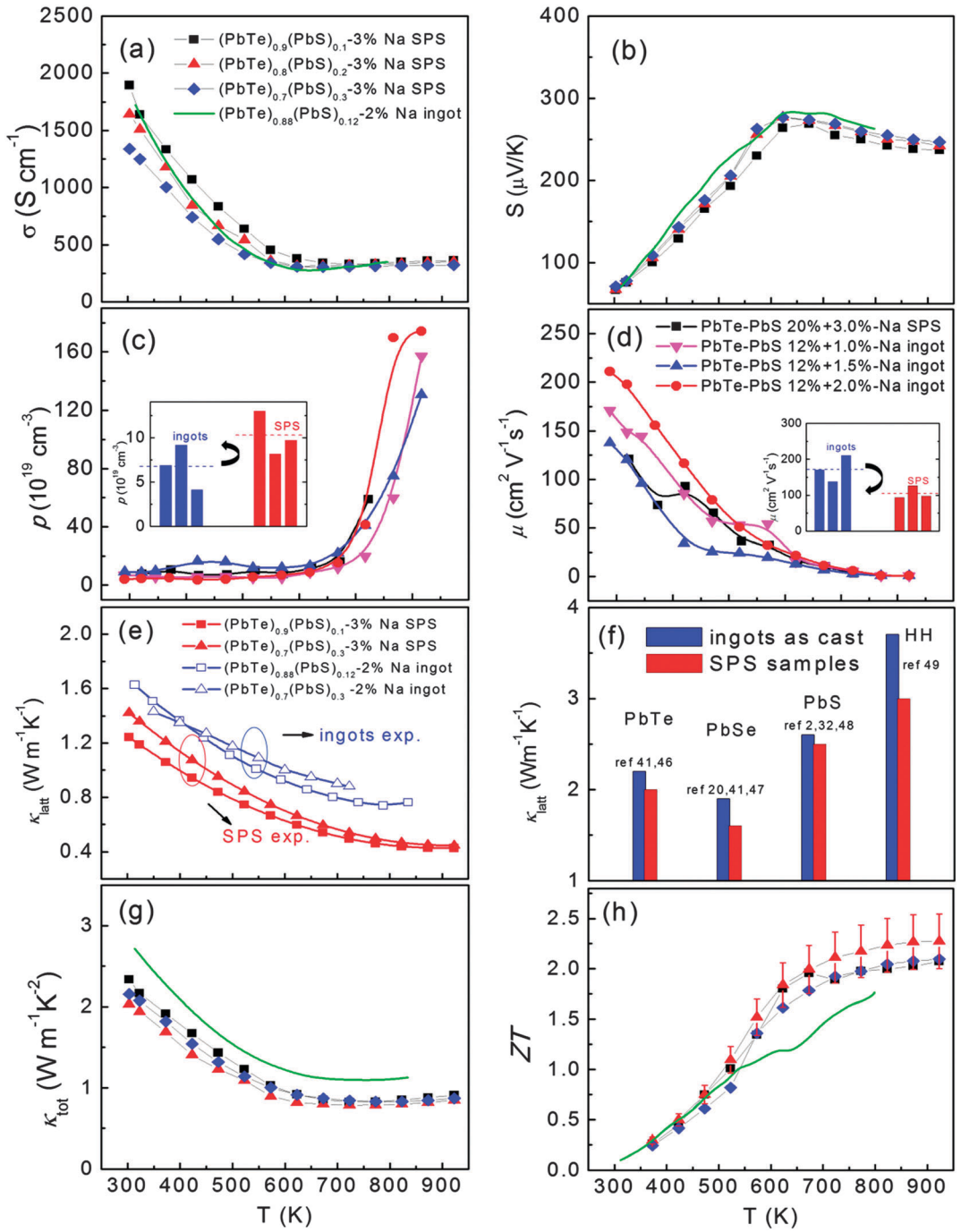

Fig. 5 (a) and (b) The very close electrical conductivities and Seebeck coefficients observed in the PbTe–PbS ingots and SPSed samples. (c) and (d) Average higher carrier concentrations and lower mobilities were found in the SPSed samples, which indicate a relatively higher level of p-type point defects therein, see Table 1. (e) Considerably lower lattice thermal conductivities were observed in the SPSed samples, (f) lower lattice thermal conductivities in highly dense SPSed samples *versus* ingots were also widely reported in other thermoelectric materials. (g) and (h) The consistently lower lattice thermal conductivities in the SPSed samples compared with ingots, which explain the observed superior overall ZT. For concision, the error bars of ZT were implemented only for the x = 20% sample.

from the Hall coefficient is superficial above 650 K and is merely the result of valence bands (L and Σ) approaching and thermally activated intrinsic electrons moving from valence bands to conduction bands. Hence, only p values at room temperature, wherein the contributions from the heavier hole Σ valence band and conduction band are diminished, are adopted in this section to give a more reliable estimation of real hole concentrations. The room temperature solubility of Na is suggested to be ~0.5 at%[41] or ~0.4 at%[45] in PbTe and ~2 at% in PbS;[41] therefore, excessive Na-doping of more than 0.5 at% should consistently lead to a hole concentration of $\sim 7.5 \times 10^{19}$ cm^{-3} ($0.5\% \times N_A\rho/M_{PbTe}$, where N_A is Avogadro's constant, ρ is mass density, and M_{PbTe} is the molecular mass of PbTe). This value is almost the same as the average hole concentrations in the three $(PbTe)_{0.88}(PbS)_{0.12}-z$ at% Na ingots, as shown in Fig. 5(c). The relatively higher concentrations of holes (correspondingly lower hole mobility, as inseted in Fig. 5(d)) in the SPSed samples indicates extra p-type doping as compared with ingots.

We undertook density functional theory (DFT) calculations as detailed in ESI,† which suggest that Pb-vacancies are the most favorable p-type point defects. Indeed, a Pb vacancy, which is highly possible to originate from the high-energy powdering and consolidation processes, is the defect with the lowest formation energy both in the PbTe and PbS phases. Considering the very similar microstructures between the all-scale hierarchical SPSed samples in this study and previously reported ingots samples,[21] we believe that these extra p-type point defects contribute, at least partly, to the consistently lower lattice thermal conductivity in the SPSed samples (Fig. 5(e)). Moreover, the inevitable grain interface barriers or slight porosity coming from the grinding and the SPS/HP processing may also be responsible for the reduced lattice thermal conductivity. This is widely reported in thermoelectrics such as PbTe,[41,46] PbSe,[20,41,47] PbS[2,32,48] and $(Zr_{0.6}Hf_{0.4})_{0.9}Ti_{0.1}NiSn$,[49] as shown in Fig. 5(f) and Table 2. The reduced carrier mobilities seen in the SPSed samples provide indirect evidence for the grain interface barriers. The further lowering of the lattice thermal conductivity results in the significantly higher ZT of the SPSed samples compared to the corresponding ingots, as shown in Fig. 5(h).

Saturation of Seebeck coefficient, S, and electrical conductivity, σ

The clearly seen saturations of the Seebeck coefficients and electrical conductivities in the Na-doped SPSed $(PbTe)_{1-x}(PbS)_x$ samples (x = 10%, 20% and 30%) start at around 600 K, as indicated by the arrows in Fig. 6(a). Saturation at a similar temperature was also reported in Na-doped $(PbTe)_{0.88}(PbS)_{0.12}$ ingots by Girard *et al.*,[21] Na-doped PbTe by Airapetyants *et al.*,[50] and Na-doped $(PbTe)_{1-x-y}(PbSe)_x(PbS)_y$ by Korkosz *et al.*[51] For comparison, the K-doped $(PbTe)_{0.7}(PbS)_{0.3}$ SPSed sample[22] exhibited smooth curves with the elevating temperature (gold solid lines); only the 3 at% K-doped sample was included in the plots for conciseness. In contrast to the relatively close charge transport values of the Na- and K-doped SPSed samples below 600 K, the discrepancies of S and σ at 900 K are as large as 25% and 50%, respectively. The saturations of S and σ in these samples apparently are crucial to maintaining the superior power factors as compared with the K-doped samples, as Fig. 6(b) shows. We argue later that the saturation phenomena arises likely from the modulated hole concentration at elevated temperatures, which is related to the further dissolution of the Na dopant. Although the hole concentrations in different samples vary (Table 1), the room temperature Seebeck coefficients are extremely close due to the domination of the lower heavier valence bands (Σ-bands) in PbTe in the case of heavy p-type doping[52] ($p > 5 \times 10^{19}$ cm^{-3}), which is further verified by the calculated Pisarenko line at 303 K (in a 2-band model), as shown Fig. 6(c). The calculations were based on the relaxation time approximated Boltzmann Transport Equation in the framework of two valence bands,[9,53] *i.e.*, upper lighter valence bands (L-bands) and Σ-bands.

For heavily doped p-type PbTe, the saturation of S and σ previously was ascribed by Airapetyants[50] to the thermal excitation of electrons from the valence to conduction bands, *i.e.*, bipolar effect, which is probably due to the coincidence of their onset temperatures. Nevertheless, this explanation was challenged by follow-up experimental values[9,54] and calculations[9,55] (including our own). The assessed concentration of thermally activated electrons at 600 K is only around ~10^{16} cm^{-3}, as seen in Fig. 6(d), which is obviously insignificant compared with the majority carrier (hole) concentration at ~10^{19} cm^{-3} and these values are consistent with calculations reported elsewhere.[52] Korkosz *et al.*[51] recently suggested that the saturation of S and σ could be explained by the topological electrons, the notion of which was proposed previously to explain the observed negative low-field Hall coefficients, R_H, in Na-doped PbTe–PbS samples at ~600 K.[52] When the initially separated L-pockets and Σ-pockets singly connect with a continuous Fermi surface, a negative curvature would form at the "neck" of the connection.

Table 1 Room temperature carrier concentrations and mobilities derived from Hall measurements for Na-doped PbTe–PbS ingots[21] and SPSed samples

Compositions	Hole concentration ($\times 10^{20}$ cm^{-3})	Hole mobility (cm^2 V^{-1} s^{-1})
1.0% Na–$(PbTe)_{0.88}(PbS)_{0.12}$ ingot	0.69	170.9
1.5% Na–$(PbTe)_{0.88}(PbS)_{0.12}$ ingot	0.92	137.7
2.0% Na–$(PbTe)_{0.88}(PbS)_{0.12}$ ingot	0.41	210.8
3.0% Na–$(PbTe)_{0.9}(PbS)_{0.1}$ SPSed	1.3	94.1
3.0% Na–$(PbTe)_{0.8}(PbS)_{0.2}$ SPSed	0.82	125.9
3.0% Na–$(PbTe)_{0.7}(PbS)_{0.3}$ SPSed	0.97	97.2

Table 2 Reported lattice thermal conductivity values (at room temperature), κ_{latt}, of SPS/HP-ed samples *versus* their corresponding ingots. Note: only hand grinding (no ball milling) was performed before the SPS/HP processes in all these cases, so as to exclude the effect of grain size; all SPS/HP-ed samples were highly consolidated (>95% at least). The unit of κ_{latt} is in W m^{-1} K^{-1}

Compositions	κ_{latt} ingots	κ_{latt} SPS/HP
PbTe	2.2[41]	2.0[46]
PbSe	1.9[41]	1.6[20,47]
PbS	2.6[2]	1.5[32,48]
$(Hf_{0.6}Zr_{0.4})_{0.9}Ti_{0.1}NiSn$	3.67[49]	3.0[49]

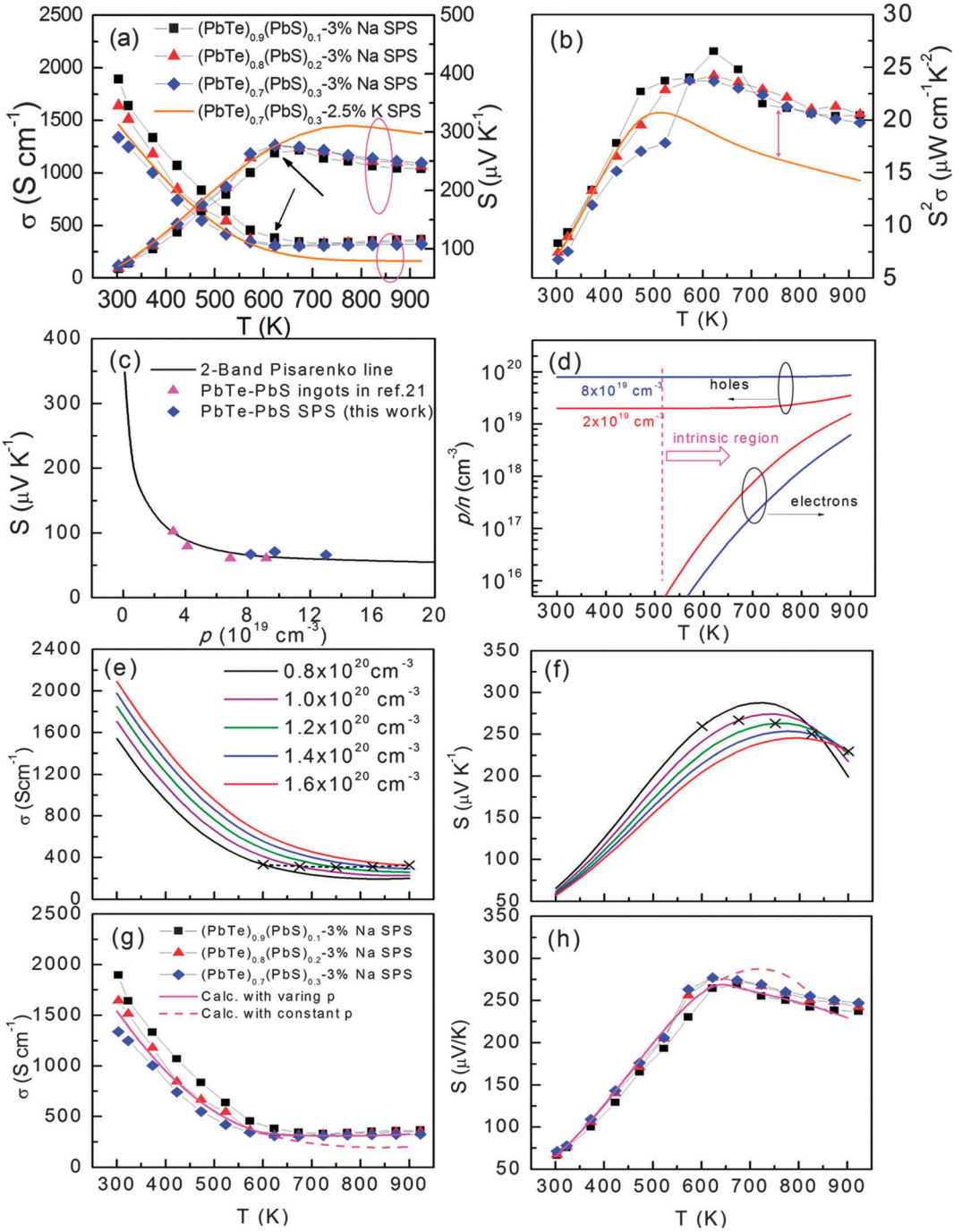

Fig. 6 (a) and (b) Saturation occurs in both electrical conductivity and the Seebeck coefficient in the Na-doped PbTe–PbS composites over ~600 K in contrast to the K-doped composites. (c) The similarity of the low-temperature Seebeck values between the Na- and K-doped SPSed samples can be explained as the contribution from the lower heavy valence bands, as the calculated Pisarenko line (303 K) shows. (d) The 3-band model calculation exhibits that the concentration of minority charge carriers (electrons) due to intrinsically thermal activation is very low at ~600 K, which is deficient to explain the observed saturation of electrical transport properties. (e) and (f) A systematical calculation of electrical conductivity and the Seebeck coefficient as hole concentration increases from 0.8 × 10^{20} to 1.6 × 10^{20} cm^{-3}. (g) and (h) Calculation (in a 3-band model) with a constant hole concentration (p = 0.8 × 10^{20} cm^{-3}) and intrinsic electrons (in dash lines) cannot explain the experiments, while that of increasing hole concentration (in solid lines) fits the measured data well.

The charge carriers in that "neck" region behave like electrons in response to a potential or a temperature gradient, and contribute negatively to the Seebeck coefficient, which is opposite to the majority of charge carriers (holes). However, this explanation might not suit our case well, since both literature[21] and our own low-field Hall measurements (−0.52 to 0.52 Tesla) of similar compositions show positive Hall coefficients as high as 823 K, in contrast to the reported negative low-field R_H of as

low as ~600 K (while, a positive R_H at higher fields). It also was argued[52] that sulfur helps in the formation of the topological connection of L and Σ bands, and thus is responsible for the onset temperature of saturation. The reason given for this was that sulfur p-orbitals could lower the L band, thus narrowing the energy gap between the two valence bands, and resulting in the contribution of topological electrons to the overall electrical transport at a lower temperature. In our understanding, since PbS has a larger energy offset between the L–Σ band edges compared with PbTe,[4] the alloying of PbS into PbTe would widen the energy gap between corresponding valence bands; moreover, observations[52] did not show a stronger sign of electron-like behavior in the 12% sulfur sample than in the 8% sample. Moreover, the topological electrons result from the "connection" of the Fermi surface of the L and Σ bands, and thus are related only with the material's intrinsic band structures; however, difficulties arise when applying this to explain the disparate electrical behaviors in Na-(obvious saturations) and K-heavily doped (no saturations were observed) $(PbTe)_{0.7}(PbS)_{0.3}$,[22] and the distinguishing trends of S and σ in Na-doped $(PbTe)_{1-x-y}(PbSe)_x(PbS)_y$ during heating and cooling cycles[51] as well.

It is interesting to note that most (if not all) of the saturation phenomena appear to take place in Na-doped samples, such as Na-doped $(PbTe)_{0.88}(PbS)_{0.12}$ by Girard *et al.*,[21] Na-doped $(PbTe)_{1-x-y}(PbSe)_x(PbS)_y$ by Korkosz *et al.*[51] and Na-doped $Pb_{0.96}Sr_{0.04}Te$ by Biswas *et al.*[14] Especially, when comparing the K-doped $(PbTe)_{0.7}(PbS)_{0.3}$ samples[22] with the Na-doped samples in this study (note that their synthetic conditions were the same, and that the hole concentrations at room temperatures are similar too), as seen in Fig. 5(a) and (b), it is natural to argue that Na is one of the key factors for the observed saturation features. Another common feature of the Na-doped samples that exhibited such saturation features is the existence of vast grain/phase boundaries or dislocations. Previously we showed that excess Na beyond the solubility limit tends to segregate at these grain/phase boundaries,[14,26] and also that the boundaries may "liquefy" at temperatures above 633 K.[56] Herein, we suggest that the saturation of S and σ results from the diffusion and re-dissolution of Na, which was confined to grain/phase boundaries at low temperatures, and back into the matrix grains at elevated temperatures. The re-dissolution of Na as p-type doping would increase the matrix hole concentration, leading to a decreased Seebeck coefficient and increased electrical conductivity.

We calculated the electrical transport properties by solving the Boltzmann Transport Equation, which accounts for the contribution from three related bands[9,53] (L + Σ valence bands along with the C conduction band) to validate our suggestion; details are given in ESI.† As seen in Fig. 6(e) and (f), electrical conductivity, σ, and the Seebeck coefficient, S, vary systematically with the elevating hole concentration from 0.8×10^{20} to 1.6×10^{20} cm^{-3}. The former value represents the measured room temperature Hall coefficient, while the latter corresponds to the high-temperature solution limit of Na in the PbTe system.[45] The onset temperature of Na diffusion at 600 K probably implies the existence of a potential energy barrier ($\sim k_B T$ = 600 K). For a better illustration, we put the calculated electrical transport properties of increasing hole concentration together with those calculated with a constant hole concentration (0.8×10^{20} cm^{-3}), and compared them with the experimental data of 3 at% Na-doped $(PbTe)_{1-x}(PbS)_x$ (x = 10%, 20% and 30%), which is shown in Fig. 6(g) and (h). If the carrier concentration is kept constant, S tends to increase smoothly to the peak around 750 K, after which it starts to decline due to the bipolar effect. The discrepancy between the calculation with a fixed hole concentration and the experimental results again points to the deficiency in Airapetyants's suggestion. In contrast, calculations with an increasing hole concentration match the experiments quite well.

The modulation of hole concentration due to the diffusion and re-dissolution of Na at elevated temperatures (over ~600 K) is beneficial to the overall thermoelectric performance; this can be understood from the viewpoint of tuning the actual carrier concentration closer to the temperature dependent optimized concentration, as argued by Pei *et al.*,[57] and as Fig. S5 (ESI†) shows. Lastly, it is also understandable that no obvious saturations were found in K-heavily doped $(PbTe)_{0.7}(PbS)_{0.3}$ since the radius of K^+ (~0.133 nm) is much larger than that of Na^+ (~0.095 nm) and it is hard for K^+ to diffuse into the matrix as a p-type dopant at elevated temperatures.

We cannot exclude the possibility that topological electrons and the bipolar effect may also contribute to the observed saturation of S and σ at high temperatures, but they do not necessarily play such a dominant role. Overall, the underlying reason is complicated and could be the combination of the elevated solubility of Na (dominating), topological electrons[51,52] and the bipolar effect;[50] while only the latter two factors might function at even higher temperatures.

Conclusions

The PbTe–PbS pseudo-binary has a complex microstructure due to the existence of an immiscibility gap between PbTe and PbS and thus exhibits very low thermal conductivity compared with its end members PbTe and PbS. We synthesized and systematically studied 3 at% Na-doped $(PbTe)_{1-x}(PbS)_x$ SPSed samples with varying PbS phase fractions x (x = 10%, 15%, 20%, 25%, 30%, and 35%). An outstanding figure of merit, ZT ~ 2.3, was obtained at 923 K when the PbS phase fraction is 20%, which corresponds to the lowest lattice thermal conductivity. The relationship between microstructure and lattice thermal conductivity was discussed based on TEM observations and theoretical calculations. Furthermore, we ascribed the consistently lower thermal conductivities in the SPSed samples (than those in the ingots) to the all-scale hierarchical architecturing. We suggested that the modulation in the hole concentration due to excessive Na diffusion and re-dissolution into the matrix grains is responsible for the observed saturations of the electrical properties over ~600 K, which result in the superior power factors in the Na-doped samples compared to those of the K-doped samples.[22]

Sample synthesis and characterization

Sample synthesis

Ingots ($\sim$20 g) with nominal compositions of $(PbTe)_{1-x}(PbS)_x$–3 at% Na (x = 10%, 15%, 20%, 25%, 30% and 35%) were synthesized by mixing the appropriate ratios of high-purity raw materials of Pb, Te, S and Na in carbon-coated quartz tubes in an N_2-filled glove box. The raw materials that were used are as follows: Pb wire (99.99%, American Elements, US), Te shot (99.999%, 5N Plus, Canada), S shot or chunk (99.999%, 5N Plus, Canada) and Na chunk (99.999%, Sigma-Aldrich, US). The quartz tubes were then evacuated to a pressure of $\sim 10^{-4}$ Torr, flame-sealed, melted at 1323 K over 10 h, and quenched to room temperature (297 K). The obtained ingots were crushed into powders and then densified by the spark plasma sintering (SPS) method (SPS-211Lx, Dr Sinter), and highly dense samples can achieve >97% of the theoretical density. To prepare for SPS processing, the melt-grown ingots were first hand-ground into powders (<5 mm^3) with a mortar and pestle, and then further ground by a mechanical mortar and pestle to reduce the grains to less than 53 μm^3. These powders were then densified at 823 K for 10 min in a 20 mm diameter graphite die under an axial compressive stress of 40 MPa. Highly dense disk-shaped pellets with the dimensions of ∅ 20 mm × 9 mm were thus obtained. The manipulations and preparation steps for powder grinding were carried out in a glove box with a purified N_2-atmosphere.

Electrical properties

The obtained pellets were cut into bars of 18 mm × 3 mm × 3 mm and used for simultaneously measuring the Seebeck coefficient and electrical conductivity with an Ulvac Riko ZEM-3 instrument under an He-atmosphere from room temperature to 923 K. The samples were coated with a thin layer (0.1–0.2 mm) of boron nitride (BN) to protect the instruments from contamination. Heating and cooling cycles gave reproducible electrical properties, thus verifying that these samples were thermally stable. The uncertainty in the Seebeck coefficient and electrical conductivity measurements is $\sim$5%. The Hall coefficients were measured using the van der Pauw technique under a reversible magnetic field of 0.52 T (8340DC, Toyo, Japan) and the uncertainty is estimated to be within 5%.

Thermal conductivity

High-density SPS processed pellets were cut and polished into coins of ∅ $\sim$ 8 mm and thickness $\sim$2 mm for measuring thermal diffusivity. The samples were coated with a thin layer of graphite to minimize errors from the emissivity of the materials. Thermal conductivity was calculated from $\kappa = D \cdot C_p \cdot \rho$, where the thermal diffusivity coefficient (D) was measured using the laser-flash diffusivity method in a Netzsch LFA457, the specific heat capacity (C_p) was indirectly derived using a representative sample (Pyroceram 9606) between 300 and 923 K, and the density (ρ) was determined using the dimensions and mass of the sample, and reconfirmed using a gas pycnometer (Micromeritics AccuPyc1340) measurement. The thermal diffusivity data were analyzed using the Cowan model with pulse correction; heating and cooling cycles gave reproducible values for every individual sample. The uncertainty of the thermal conductivity is estimated to be within 5%, considering the uncertainties for D, C_p, and ρ. The combined uncertainty for all measurements involved in the calculation of ZT is about 15%.

Electron microscopy

S/TEM investigations were carried out in an aberration-corrected JEOL ARM200 microscope operated at 200 kV. Thin TEM specimens were prepared by conventional standard methods. These procedures included cutting, grinding, dimpling, polishing, and Ar-ion milling with a liquid nitrogen cooling stage. SEM investigations were performed using a Zeiss Merlin microscope, and SEM specimens were meticulously polished before examination under the microscope.

X-ray diffraction

Powdery X-ray diffraction patterns were performed using a Smartlab (9 kW, Rigaku, Japan), the powders were obtained *via* hand-milling in a mechanical mortar and pestle to a grain size no more than 53 μm^3.

Acknowledgements

This contribution was supported by the startup of South University of Science and Technology of China, and partly supported by the Science, Technology and Innovation Commission of Shenzhen Municipality (Grant No. JCYJ20140612140151884), the NSFC under Grant No. 11404160 (Li Huang), the "Zhuoyue program" from Beihang University and the Recruitment Program for Young Professionals (L-D. Zhao), the NSFC under Grant No. 51202008, and the Postdoctoral Science Foundation of China (2013M540037) (Y.L. Pei). At Northwestern, the study was supported as part of the Revolutionary Materials for Solid State Energy Conversion, an Energy Frontier Research Center funded by the U.S. Department of Energy, Office of Science, and Office of Basic Energy Sciences under Award Number DE-SC0001054. D. Wu would like to thank Haijun Wu and Fengshan Zheng for their thoughtful discussions on this manuscript.

References

1 D. M. Rowe, *CRC handbook of thermoelectrics*, CRC press, 1995.
2 Y. I. Ravich, *Semiconducting Lead Chalcogenides*, Plenum, 1970.
3 Y. Pei, H. Wang and G. J. Snyder, *Adv. Mater.*, 2012, **24**, 6125–6135.
4 Z. M. Gibbs, H. Kim, H. Wang, R. L. White, F. Drymiotis, M. Kaviany and G. Jeffrey Snyder, *Appl. Phys. Lett.*, 2013, **103**, 262109.
5 E. S. Božin, C. D. Malliakas, P. Souvatzis, T. Proffen, N. A. Spaldin, M. G. Kanatzidis and S. J. Billinge, *Science*, 2010, **330**, 1660–1663.

6 O. Delaire, J. Ma, K. Marty, A. F. May, M. A. McGuire, M. H. Du, D. J. Singh, A. Podlesnyak, G. Ehlers, M. D. Lumsden and B. C. Sales, *Nat. Mater.*, 2011, **10**, 614–619.
7 J. P. Heremans, V. Jovovic, E. S. Toberer, A. Saramat, K. Kurosaki, A. Charoenphakdee, S. Yamanaka and G. J. Snyder, *Science*, 2008, **321**, 554–557.
8 J. P. Heremans, B. Wiendlocha and A. M. Chamoire, *Energy Environ. Sci.*, 2012, **5**, 5510.
9 Y. Pei, X. Shi, A. LaLonde, H. Wang, L. Chen and G. J. Snyder, *Nature*, 2011, **473**, 66–69.
10 (*a*) L. D. Zhao, H. J. Wu, S. Q. Hao, C. I. Wu, X. Y. Zhou, K. Biswas, J. Q. He, T. P. Hogan, C. Uher, C. Wolverton, V. P. Dravid and M. G. Kanatzidis, *Energy Environ. Sci.*, 2013, **6**, 3346; (*b*) X. Zhang and L. D. Zhao, *Journal of Materiomics*, DOI: 10.1016/j.jmat.2015.01.001.
11 H. Wang, J. Wang, X. Cao and G. J. Snyder, *J. Mater. Chem. A*, 2014, **2**, 3169.
12 Y. Pei, H. Wang, Z. M. Gibbs, A. D. LaLonde and G. J. Snyder, *NPG Asia Mater.*, 2012, **4**, e28.
13 J. He, M. G. Kanatzidis and V. P. Dravid, *Mater. Today*, 2013, **16**, 166–176.
14 K. Biswas, J. He, I. D. Blum, C. I. Wu, T. P. Hogan, D. N. Seidman, V. P. Dravid and M. G. Kanatzidis, *Nature*, 2012, **489**, 414–418.
15 Y. Pei, J. Lensch-Falk, E. S. Toberer, D. L. Medlin and G. J. Snyder, *Adv. Funct. Mater.*, 2011, **21**, 241–249.
16 J. Martin, G. Nolas, W. Zhang and L. Chen, *Appl. Phys. Lett.*, 2007, **90**, 222112.
17 H. Wu, J. Carrete, Z. Zhang, Y. Qu, X. Shen, Z. Wang, L.-D. Zhao and J. He, *NPG Asia Mater.*, 2014, **6**, e108.
18 C.-H. Kuo, H.-S. Chien, C.-S. Hwang, Y.-W. Chou, M.-S. Jeng and M. Yoshimura, *Mater. Trans.*, 2011, **52**, 795–801.
19 J. L. Wang, H. Wang, G. J. Snyder, X. Zhang, Z. H. Ni and Y. F. Chen, *J. Phys. D: Appl. Phys.*, 2013, **46**, 405301.
20 Q. Zhang, F. Cao, W. Liu, K. Lukas, B. Yu, S. Chen, C. Opeil, D. Broido, G. Chen and Z. Ren, *J. Am. Chem. Soc.*, 2012, **134**, 10031–10038.
21 S. N. Girard, J. He, X. Zhou, D. Shoemaker, C. M. Jaworski, C. Uher, V. P. Dravid, J. P. Heremans and M. G. Kanatzidis, *J. Am. Chem. Soc.*, 2011, **133**, 16588–16597.
22 H. J. Wu, L. D. Zhao, F. S. Zheng, D. Wu, Y. L. Pei, X. Tong, M. G. Kanatzidis and J. Q. He, *Nat. Commun.*, 2014, **5**, 4515.
23 J. Androulakis, I. Todorov, J. He, D. Y. Chung, V. Dravid and M. Kanatzidis, *J. Am. Chem. Soc.*, 2011, **133**, 10920–10927.
24 V. Leute and N. Volkmer, *Z. Phys. Chem.*, 1985, **144**, 145–155.
25 S. N. Girard, J. He, C. Li, S. Moses, G. Wang, C. Uher, V. P. Dravid and M. G. Kanatzidis, *Nano Lett.*, 2010, **10**, 2825–2831.
26 J. He, I. D. Blum, H. Q. Wang, S. N. Girard, J. Doak, L. D. Zhao, J. C. Zheng, G. Casillas, C. Wolverton, M. Jose-Yacaman, D. N. Seidman, M. G. Kanatzidis and V. P. Dravid, *Nano Lett.*, 2012, **12**, 5979–5984.
27 S. N. Girard, K. Schmidt-Rohr, T. C. Chasapis, E. Hatzikraniotis, B. Njegic, E. M. Levin, A. Rawal, K. M. Paraskevopoulos and M. G. Kanatzidis, *Adv. Funct. Mater.*, 2013, **23**, 747–757.
28 L. D. Zhao, V. P. Dravid and M. G. Kanatzidis, *Energy Environ. Sci.*, 2014, **7**, 251.
29 J. He, S. N. Girard, M. G. Kanatzidis and V. P. Dravid, *Adv. Funct. Mater.*, 2010, **20**, 764–772.
30 H. Wang, J. H. Bahk, C. Kang, J. Hwang, K. Kim, J. Kim, P. Burke, J. E. Bowers, A. C. Gossard, A. Shakouri and W. Kim, *Proc. Natl. Acad. Sci. U. S. A.*, 2014, **111**, 10949–10954.
31 S. Johnsen, J. He, J. Androulakis, V. P. Dravid, I. Todorov, D. Y. Chung and M. G. Kanatzidis, *J. Am. Chem. Soc.*, 2011, **133**, 3460–3470.
32 H. Wang, E. Schechtel, Y. Pei and G. J. Snyder, *Adv. Energy Mater.*, 2013, **3**, 488–495.
33 D. M. Rowe and C. Bhandari, *Modern thermoelectrics*, Prentice Hall, 1983.
34 D. Wu, Y. Pei, Z. Wang, H. Wu, L. Huang, L.-D. Zhao and J. He, *Adv. Funct. Mater.*, 2014, **24**, 7763–7771.
35 Y. K. Koh, C. Vineis, S. Calawa, M. Walsh and D. G. Cahill, *Appl. Phys. Lett.*, 2009, **94**, 153101.
36 K. F. Hsu, S. Loo, F. Guo, W. Chen, J. S. Dyck, C. Uher, T. Hogan, E. K. Polychroniadis and M. G. Kanatzidis, *Science*, 2004, **303**, 818–821.
37 L.-D. Zhao, S.-H. Lo, Y. Zhang, H. Sun, G. Tan, C. Uher, C. Wolverton, V. P. Dravid and M. G. Kanatzidis, *Nature*, 2014, **508**, 373–377.
38 A. J. Minnich, M. S. Dresselhaus, Z. F. Ren and G. Chen, *Energy Environ. Sci.*, 2009, **2**, 466.
39 J. W. Doak and C. Wolverton, *Phys. Rev. B: Condens. Matter Mater. Phys.*, 2012, **86**, 144202.
40 J. He, J. Androulakis, M. G. Kanatzidis and V. P. Dravid, *Nano Lett.*, 2012, **12**, 343–347.
41 J. He, L. D. Zhao, J. C. Zheng, J. W. Doak, H. Wu, H. Q. Wang, Y. Lee, C. Wolverton, M. G. Kanatzidis and V. P. Dravid, *J. Am. Chem. Soc.*, 2013, **135**, 4624–4627.
42 D. L. Medlin and G. J. Snyder, *Curr. Opin. Colloid Interface Sci.*, 2009, **14**, 226–235.
43 A. Minnich and G. Chen, *Appl. Phys. Lett.*, 2007, **91**, 073105.
44 D. Wu, A. S. Petersen and S. J. Poon, *AIP Adv.*, 2013, **3**, 082116.
45 S. A. Yamini, T. Ikeda, A. Lalonde, Y. Pei, S. X. Dou and G. J. Snyder, *J. Mater. Chem. A*, 2013, **1**, 8725.
46 A. D. LaLonde, Y. Pei and G. J. Snyder, *Energy Environ. Sci.*, 2011, **4**, 2090.
47 H. Wang, Y. Pei, A. D. LaLonde and G. J. Snyder, *Proc. Natl. Acad. Sci. U. S. A.*, 2012, **109**, 9705–9709.
48 L. D. Zhao, S. H. Lo, J. He, H. Li, K. Biswas, J. Androulakis, C. I. Wu, T. P. Hogan, D. Y. Chung, V. P. Dravid and M. G. Kanatzidis, *J. Am. Chem. Soc.*, 2011, **133**, 20476–20487.
49 K. Kurosaki, T. Maekawa, H. Muta and S. Yamanaka, *J. Alloys Compd.*, 2005, **397**, 296–299.
50 S. Airapetyants, M. Vinogradova, I. Dubrovskaya, N. Kolomoets and I. Rudnik, *Sov. Phys. Solid State*, 1966, **8**, 1069–1072.
51 R. J. Korkosz, T. C. Chasapis, S. H. Lo, J. W. Doak, Y. J. Kim, C. I. Wu, E. Hatzikraniotis, T. P. Hogan, D. N. Seidman, C. Wolverton, V. P. Dravid and M. G. Kanatzidis, *J. Am. Chem. Soc.*, 2014, **136**, 3225–3237.

52 C. M. Jaworski, M. D. Nielsen, H. Wang, S. N. Girard, W. Cai, W. D. Porter, M. G. Kanatzidis and J. P. Heremans, *Phys. Rev. B: Condens. Matter Mater. Phys.*, 2013, **87**, 045203.
53 (*a*) D. Wu, L. D. Zhao, S. Hao, Q. Jiang, F. Zheng, J. W. Doak, H. Wu, H. Chi, Y. Gelbstein, C. Uher, C. Wolverton, M. Kanatzidis and J. He, *J. Am. Chem. Soc.*, 2014, **136**, 11412–11419; (*b*) H. J. Wu, F. S. Zheng, D. Wu, Z. H. Ge, X. Y. Liu and J. He, *Nano Energy*, 2015, **13**, 626–650.
54 Y. Pei, A. LaLonde, S. Iwanaga and G. J. Snyder, *Energy Environ. Sci.*, 2011, **4**, 2085.
55 Y. Pei, H. Wang and G. J. Snyder, *Adv. Mater.*, 2012, **24**, 6125–6135.
56 S. A. Yamini, T. Ikeda, A. Lalonde, Y. Pei, S. X. Dou and G. J. Snyder, *J. Mater. Chem. A*, 2013, **1**, 8725–8730.
57 Y. Pei, A. D. LaLonde, N. A. Heinz, X. Shi, S. Iwanaga, H. Wang, L. Chen and G. J. Snyder, *Adv. Mater.*, 2011, **23**, 5674–5678.